metals

MDPI

Article

Analysis of Hydrogen-Induced Changes in the Cyclic Deformation Behavior of AISI 300–Series Austenitic Stainless Steels Using Cyclic Indentation Testing

Sven Brück [1], Bastian Blinn [2,*], Katharina Diehl [1], Yannick Wissing [1], Julian Müller [1], Martina Schwarz [3], Hans-Jürgen Christ [1], Tilmann Beck [2], Thorsten Staedler [1], Xin Jiang [1], Benjamin Butz [1] and Stefan Weihe [3]

[1] Institut für Werkstofftechnik, Universität Siegen, Paul-Bonatz-Straße 9-11, 57076 Siegen, Germany; sven.brueck@uni-siegen.de (S.B.); katharina.diehl@uni-siegen.de (K.D.); yannickwissing@web.de (Y.W.); julian.mueller@uni-siegen.de (J.M.); Hans-Juergen.Christ@uni-siegen.de (H.-J.C.); thorsten.staedler@uni-siegen.de (T.S.); xin.jiang@uni-siegen.de (X.J.); benjamin.butz@uni-siegen.de (B.B.)

[2] Institute of Materials Science and Engineering, TU Kaiserslautern, Post Office Box 3049, 67653 Kaiserslautern, Germany; beck@mv.uni-kl.de

[3] Materialprüfungsanstalt Stuttgart, Universität Stuttgart, Pfaffenwaldring 9, 70569 Stuttgart, Germany; martina.schwarz@mpa.uni-stuttgart.de (M.S.); stefan.weihe@imwf.uni-stuttgart.de (S.W.)

* Correspondence: blinn@mv.uni-kl.de; Tel.: +49-631-205-5288

Abstract: The locally occurring mechanisms of hydrogen embrittlement significantly influence the fatigue behavior of a material, which was shown in previous research on two different AISI 300-series austenitic stainless steels with different austenite stabilities. In this preliminary work, an enhanced fatigue crack growth as well as changes in crack initiation sites and morphology caused by hydrogen were observed. To further analyze the results obtained in this previous research, in the present work the local cyclic deformation behavior of the material volume was analyzed by using cyclic indentation testing. Moreover, these results were correlated to the local dislocation structures obtained with transmission electron microscopy (TEM) in the vicinity of fatigue cracks. The cyclic indentation tests show a decreased cyclic hardening potential as well as an increased dislocation mobility for the conditions precharged with hydrogen, which correlates to the TEM analysis, revealing courser dislocation cells in the vicinity of the fatigue crack tip. Consequently, the presented results indicate that the hydrogen enhanced localized plasticity (HELP) mechanism leads to accelerated crack growth and change in crack morphology for the materials investigated. In summary, the cyclic indentation tests show a high potential for an analysis of the effects of hydrogen on the local cyclic deformation behavior.

Keywords: hydrogen embrittlement; cyclic indentation tests; nanoindentation; hydrogen enhanced localized plasticity (HELP); dislocation arrangements

Citation: Brück, S.; Blinn, B.; Diehl, K.; Wissing, Y.; Müller, J.; Schwarz, M.; Christ, H.-J.; Beck, T.; Staedler, T.; Jiang, X.; et al. Analysis of Hydrogen-Induced Changes in the Cyclic Deformation Behavior of AISI 300–Series Austenitic Stainless Steels Using Cyclic Indentation Testing. *Metals* **2021**, *11*, 923. https://doi.org/10.3390/met11060923

Academic Editor: Antonio Mateo

Received: 11 May 2021
Accepted: 3 June 2021
Published: 6 June 2021

1. Introduction

As renewable energy and the sustainable conversion of energy become more important, high conversion efficiency offers promising advantages for mobile and stationary applications. In these areas stainless steels are often used, which show a tendency to hydrogen embrittlement, as exemplarily reported in the overview work of Lynch [1]. To ensure safe dimensioning of components for these applications, it is necessary to characterize the hydrogen-induced changes in the material properties, and especially, the fatigue behavior. In the literature several mechanisms are presented, which explain hydrogen embrittlement by different concepts, i.e., hydrogen enhanced localized plasticity (HELP), hydrogen enhanced decohesion (HEDE), and adsorption induced dislocation emission (AIDE). These mechanisms are briefly explained below and shown schematically in Figure 1. They can occur separately as well as combined during different stages of fatigue crack growth, whereby the dominant damage mechanism can change [1].

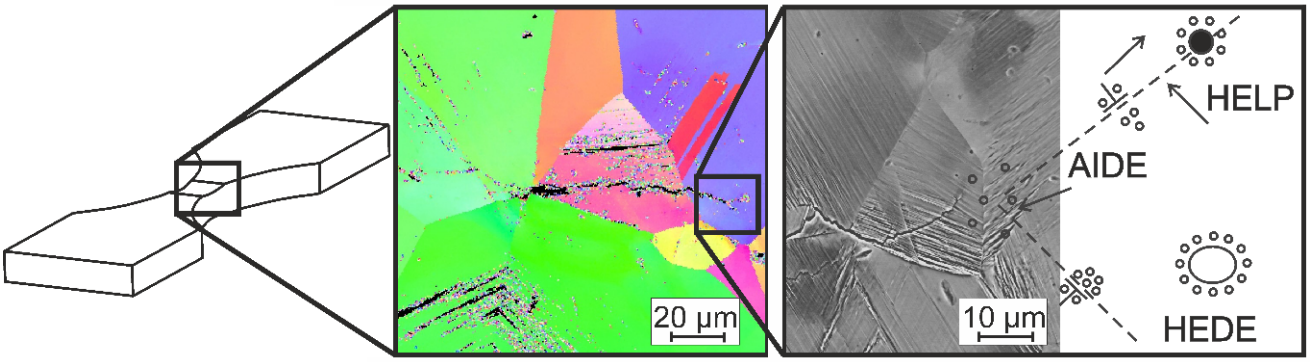

Figure 1. Schematic representation of the main mechanisms for hydrogen embrittlement.

The HELP mechanism was proposed by Beachem [2] and assumes that hydrogen leads to an accelerated dislocation motion. Hydrogen behaves as a Cotrell cloud inside the stress field of a dislocation, shielding the dislocation from the distorted lattice. This effect causes a reduction of the interaction energy between the dislocation and obstacles [3], resulting in a decreasing external stress level required for dislocation movement [4].

The HEDE mechanism is based on the weakening effect of the accumulated hydrogen on interatomic metal bonds. Localized accumulations of hydrogen preferentially occur in elastically strained areas, e.g., at grain and phase boundaries as well as near crack tips. As the hydrogen results in a decreased binding energy, separation of single bonds can occur, which is defined as decohesion [1]. This mechanism is responsible for the preferential growth of hydrogen-induced cracks along grain boundaries, phase boundaries or other areas of microstructural disorder.

The AIDE mechanism is much more complex than the previously mentioned mechanisms and has been explained differently over time. The oldest work of Petch and Stables [5] from 1952 explains this mechanism thermodynamically by the binding of hydrogen to free surfaces, such as pores or cracks as well as the outer surface. Furthermore, in [6,7] it is reported that hydrogen leads to a reduction of the surface energy γ_{OF}. Lynch [8–11] has been developing the AIDE mechanism since the 1970s and postulates that the hydrogen at the crack tip facilitates the emission of dislocations. Lynch argues that the adsorption of hydrogen at the crack tip, rather than the hydrogen in solution before the crack tip, increases the dislocation emission and leads to local plasticity.

By analyzing the different hydrogen mechanisms, it has to be considered that they can be active simultaneously [1]. As discussed by Lynch [1], the dominating mechanism can change during the fatigue lifetime. Thereby, the material condition, the local microstructure, the stress intensity, as well as the environmental conditions significantly influence which mechanism dominates [1]. In correspondence to that, Wang et al. [12] observed at austenitic stainless steel 304 L that deformation-induced austenite α'-martensite transformation, which was introduced by pre-loading, promotes the activity of HEDE. In this work [12], it is further assumed that the HELP mechanism locally leads to an enhanced plasticity, which results in more pronounced phase transformation and accumulation of dislocations at obstacles (e.g., grain boundaries), leading to a local increase of hydrogen content and finally to crack initiation caused by decohesion (HEDE). In correspondence to Lynch [1], Li et al. [13] reported for the same kind of steel a simultaneous activity of HELP and AIDE at sufficient hydrogen contents. Moreover, in their overview work, Djukic et al. [14] reported a combined activity of HEDE and HELP, whereby the change in the dominating effect correlates with changes in the fracture surface.

As discussed in [14], the hydrogen content significantly influences which type of hydrogen mechanism is active, whereby at medium hydrogen contents the HELP mechanism seems to be antecedent to the HEDE mechanism, while at higher amounts of hydrogen the HEDE mechanism occurs solely. Thereby, also the type of hydrogen charging has to

be considered, as for example, an electrochemical charging results in higher hydrogen contents in relation to gaseous charging [15].

In addition to the shown mechanism, the presence of hydrogen leads to a decreased stacking fault energy γ_{SF}, which is a crucial factor to describe the tendency to phase transformation. Thus, the influence of hydrogen precharging on the transformation of γ (austenite) into α'-martensite has to be analyzed. Moreover, Weidner and Biermann [16] demonstrated that the slip planarity is dependent on γ_{SF}, whereby an increasing γ_{SF} supports cross slip and lower γ_{SF} provides planary slip. The detailed transmission electron microscope (TEM) examination reported by Robertson et al. [17] showed that hydrogen facilitates dislocation motion and decreases γ_{SF}, impeding cross slip. In addition to that, Gerberich et al. [18] showed a hydrogen-induced reduction of the stress, which is necessary for dislocation formation and movement.

To analyze the influence of hydrogen on the mechanical properties at a smaller length scale, several researchers used indentation testing [19–25], reporting higher hardness and less pronounced plastic deformation for hydrogen precharged materials. In addition to the conventional hardness measurement, instrumented indentation tests can be used to characterize the elastic properties of a material [26,27]. Moreover, this testing method can be carried out cyclically and therefore, can be utilized to investigate fatigue properties. Xu et al. [28,29] were one of the first groups to present the possibility of analyzing the fatigue behavior with cyclic indentation testing. They showed that the propagation of indentation depth and resulting calculations of stress intensity are comparable to the results obtained in fatigue tests. In addition, Saraswati et al. [30] described the cyclic deformation behavior of 5 N pure Au and Ca-doped Au rods via cyclic nanoindentation testing. Furthermore, Kramer et al. [31] developed a force controlled method based on instrumented cyclic indentation, which is known as PhyBaL$_{CHT}$ and enables the characterization of the cyclic properties of a material, i.e., the cyclic hardening potential. Based on this method, Görzen et al. [32] demonstrated that the cyclic hardening potential obtained in cyclic indentation tests correlates well with the defect tolerance of a material. As shown by Nix and Gao [33], Durst et al. [34], and Sadrabadi et al. [35], the plastically deformed zone beneath the indenter, and therefore, the investigated volume, depends on the size of the indentation diagonal. Consequently, a lower indentation force is needed to examine the cyclic deformation behavior at smaller length scales, as shown by Blinn et al. [36] at differently heat-treated variants of 42CrMo4 and 18CrNiMo7-6 steel. With decreasing indent diagonals (less than 5 µm), an increasing influence of local microstructural inhomogeneities and thus, a higher spatial resolution was observed in this work [36].

In previously published fatigue tests on AISI 300-series austenitic stainless steels the presence of hydrogen led to an earlier crack initiation and a change of the crack initiation site, as well as crack morphology [4]. Moreover, the hydrogen resulted in higher extruded slip bands, showing a wider distance between each other in relation to the slip band observed at the hydrogen-free reference condition. This could be explained by the HELP mechanism in terms of a more localized and stronger plastic deformation [4]. Based on these results, the experimental approaches used in the presented work focus on the effects within the plastic zone in front of a fatigue crack, where the HELP mechanism is assumed to be active. For this purpose, two kinds of indentation tests were applied at two different variants of AISI 304-type austenitic stainless steel, being investigated in [4]. These indentation tests enable the characterization of the mechanical properties and cyclic deformation behavior at the microscale (PhyBaL$_{CHT}$) and nanoscale (nanoindentation fatigue tests). Combined with the results from fatigue tests [4] as well as TEM analyses conducted at the fatigue specimens, the influence of hydrogen on the mechanical properties can be analyzed at different length scales. Moreover, this approach enables an evaluation of the applicability of cyclic indentation testing for local analysis of hydrogen effects on the cyclic deformation behavior.

2. Materials and Methods

2.1. Materials

In the present work, two metastable austenitic stainless steels of type AISI 304 with different Ni contents were investigated (see Table 1). According to the Ni content, the Ni-lean (about 9 wt%) and the Ni-rich (about 12 wt%) alloy will be named X2-9 and X2-12 in the following. The different Ni contents lead to different austenite stabilities and hence, differently pronounced transformation from γ-austenite into α'-martensite [4], which significantly influences the fatigue behavior [37,38]. The materials exhibit a homogeneous microstructure with a grain size of approximately 150–200 µm. Despite Ni contents of 9.07 and 12.36 wt%, both steels feature a metastable austenitic microstructure. The susceptibility of the transformation from γ to α'-martensite can be characterized by M_{d30}, which can be calculated in °C according to Equation (1) [39]. M_{d30} is the temperature at which 50% of the initial austenitic phase is transformed into α'-martensite by a plastic deformation of 30%. Consequently, the higher the M_{d30}, the less stable the austenitic phase of the material. Moreover, the austenite stability correlates to the γ_{SF} value, which is calculated in J/m^2 by Equation (2) [40].

$$M_{d30} = 413 - 462\,(\text{wt\% C} + \text{wt\% N}) - 9.2\ \text{wt\% Si} - 8.1\ \text{wt\% Mn} - 13.7\ \text{wt\% Cr} - 20\ \text{wt\% Ni} - 18.5\ \text{wt\% Mo} \quad (1)$$

$$\gamma_{SF} = -53 + 6.2\ \text{wt\% Ni} + 0.7\ \text{wt\% Cr} + 3.2\ \text{wt\% Mn} + 9.3\ \text{wt\% Mo} \quad (2)$$

Table 1. Chemical composition of investigated metastable austenitic steels X2-9 and X2-12.

Elements in wt%	C	Si	Mn	Cr	Mo	Nb	Ni	N	Ti
X2-9	0.014	0.53	1.71	18.05	0.02	0.01	9.07	0.016	0.005
X2-12	0.016	0.48	1.75	17.78	0.02	0.01	12.36	0.017	0.005

The M_{d30} of X2-9 and of X2-12 is −48.64 and −111.99 °C, respectively, and the γ_{SF} values were calculated to be 21.52 J/m^2 for X2-9 and 41.86 J/m^2 for X2-12. The calculated values as well as the Schaeffler diagram [4] indicate that X2-9 has a stronger tendency towards phase transformation than X2-12. As documented in previous investigations [4], X2-12 does not show any phase transformation at cyclic loading, whereas X2-9 exhibits a significant formation of plastic deformation-induced α'-martensite in fatigue tests.

To analyze the influence of hydrogen on the mechanical properties, for each material a hydrogen-free reference condition as well as a condition precharged with hydrogen were investigated. Hydrogen-precharging, which was conducted at the Materialprüfungsanstalt (MPA) Stuttgart (Germany), was done from the gas phase (473 K, 180 bar, H_2 gas of 99.9999% purity, 28 days), resulting in a hydrogen content of about 40 wppm for X2-12 and 26 wppm for X2-9. The given hydrogen contents were determined by melt extraction (LECO 836H). Note that melt extraction only provides information of the hydrogen content in the whole volume investigated and thus, does not enable a local analysis. However, in preliminary work, after 28 days no further increase of hydrogen content was measured in the volume and hence, a nearly homogenous distribution of hydrogen between the surface region and the inner volume of the specimen is expected. Moreover, no effusion of hydrogen is assumed during the mechanical testing, as a storage at laboratory air for 28 days did not lead to a reduction of the measured hydrogen content, which is a significantly longer time than test durations and time between charging and testing.

2.2. Fatigue Tests

The fatigue tests and their results presented here are taken from previous work described in detail in [4]. For the convenience of the reader, the tests and the relevant results obtained are summarized in this paper.

The fatigue tests were performed in laboratory air at 20 °C with a servo-hydraulic testing system and an electromechanical miniature testing machine mounted in a confocal laser microscope. Fatigue loading was applied in stress control at a stress ratio of $R = -1$ using stress amplitudes of σ_a = 365 MPa (X2-12, precharged (H_2) and reference samples (ref)), σ_a = 430 MPa (X2-9, precharged samples (H_2)) and σ_a = 460 MPa (X2-9, reference samples (ref)) in sinusoidal waveform with a frequency of f = 1 Hz. Using far field microscopy, the initiation and growth of microstructurally short fatigue cracks were monitored in the servo-hydraulic testing system. The experiments on the miniature testing machine were carried out quasi in situ with a confocal laser microscope (Olympus LEXT3000). For this purpose, images of the specimen surfaces were taken in fixed intervals (5000 cycles) and later evaluated with regards to the reconstruction of the crack initiation site and crack propagation. The investigations of fracture surfaces and microstructures were carried out on a FEI Helios Dual Beam focused ion beam (FIB)/scanning electron microscope (SEM), while the topographic surface measurements were carried out with the abovementioned confocal laser microscope.

2.3. *PhyBaL*$_{CHT}$

To characterize the cyclic deformation behavior of the different material conditions, cyclic indentation tests were performed with a Fischerscope H100C and additionally with a Hysitron Triboindenter, which offers a higher spatial resolution. Both testing devices enable a continuous measurement of the indentation depth h and the indentation force F. In the cyclic indentation tests carried out with the Fischerscope H100C, the material was cyclically loaded by a Vickers indenter at a frequency of $f = 1/12$ Hz and a maximum indentation force of F_{max} = 1000 mN, while in experiments with Hysitron Triboindenter a frequency of f = 1 Hz, a Berkovich indenter, and a maximum load of F_{max} = 5 mN were used.

For determination of the cyclic deformation behavior, 10 load cycles were applied at each indentation point. From the 2nd cycle on, an *F*-*h* hysteresis loop can be observed [31,36]. In accordance with the plastic strain amplitude $\varepsilon_{a,p}$, determined from stress-strain hysteresis loops in uniaxial fatigue tests, the half width at mean loading is defined as plastic indentation depth amplitude $h_{a,p}$, which is used to describe the cyclic deformation behavior [31,36]. Therefore, the $h_{a,p}$ values are plotted against the number of cycles and the resulting $h_{a,p}$-N curves are analyzed. Starting from the 5th cycle, the $h_{a,p}$-N curve exhibits a change in slope, indicating that macroplastic deformation processes become saturated and microplastic deformation dominates the cyclic deformation behavior [31,36]. Furthermore, the regime after the 5th cycle can be described by a power law function $h_{a,p\ II}$ (see Equation (3)), whereby its exponent e_{II} is called the cyclic hardening exponent$_{CHT}$ [31,36].

$$h_{a,p\ II} = a_{II} \cdot N^{\,e_{II}} \tag{3}$$

Note that a steeper slope of the $h_{a,p}$-N curve is caused by a more pronounced cyclic hardening. Since the cyclic hardening exponent$_{CHT}$ describes the slope of $h_{a,p}$-N curve after the 5th cycle, a higher $|e_{II}|$ represents a higher cyclic hardening potential.

In addition to the analysis of the cyclic deformation behavior, the indentation depth observed in the first cycle was used to determine the Martens hardness (*HM*) of the material, which serves as a reference value for the monotonic strength on the microscale.

In previously published work [31,36], this short-time procedure is explained in more detail.

To obtain statistically reliable results, for each condition a minimum number of 20 indentation points were used for the determination of mean values of *HM*, e_{II}, and $h_{a,p}$. Note that the deviations shown in Section 3.2 represent the confidence intervals of 90%.

2.4. Nanoindentation Fatigue Tests

More dynamic nanoindentation fatigue tests were performed up to a number of loading cycles far in excess of the 10 cycles used in the PhyBaL$_{CHT}$ approach. Moreover, significantly lower indentation forces were required to characterize the cyclic deformation

behavior at nanoscale. Consequently, the indenter was subjected to a quasi-static load of 100 µN, which was superimposed by a sinusoidal amplitude of 80 µN at a frequency of 220 Hz for 8×10^5 cycles.

In these indentation tests, the measurement of the total indentation depth was not possible. However, by determining the contact modulus at the beginning of the tests and continuous monitoring of the stiffness, the displacement amplitude was obtained. Note that in the presented work, no significant influence of thermal drift on the test results was observed.

During the indentation fatigue tests abrupt changes in the displacement amplitude (further called *events*) were observed and determined by means of the MATLAB function "findchangepts". These *events* were used in accordance with Faisal et al. [41] to characterize the deformation processes at the nanoscale. To provide statistically reliable data, these tests were made at 10 different positions for both, X2-9 as well as X2-12 samples (reference (ref) and precharged (H_2) conditions), separated by at least 100 µm to avoid interaction phenomena.

2.5. TEM Investigations

Transmission electron microscopy (TEM) samples were prepared using the focused Ga ion beam of a Dual Beam Microscope of type Helius Nanolab 600. Samples were cut from the areas ahead of the crack tip of fatigue cracks (see Figure 2). Before the foils were lifted out, they were polished with an ion beam energy of 2 kV.

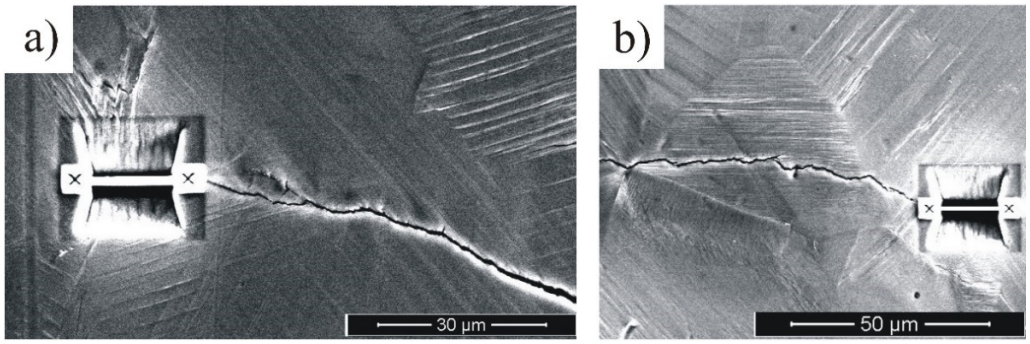

Figure 2. TEM samples of (**a**) X2-12 ref and (**b**) X2-12 H2, prepared with FIB.

The TEM characterization of the microstructure was done with a FEI Talos F200X, using an acceleration voltage of 200 kV. Bright field and dark field imaging were employed to investigate the defect structure. Additionally, scanning TEM (STEM) overview images were taken to illustrate the position of the crack tip.

3. Results

3.1. Previous Fatigue Tests

In this section, the results of fatigues tests already reported in detail in [4], and being relevant for the presented work, are summarized compactly.

The fatigue tests reveal no clear influence of hydrogen on the crack growth rate for X2-12 (see Figure 3a). However, after fatigue testing, significant differences between precharged and reference conditions were revealed in the microstructure: Whereas the reference specimens exhibit crack initiation at slip bands and grain boundaries, grain boundary triple points served as crack initiation sites for precharged specimens (see Figure 4). Moreover, the crack morphology of precharged specimens is characterized by alternating slip in rather clearly defined slip systems as well as crack tip branching, which leads to a ramified crack path. In contrast to that, short cracks in reference specimens follow the slip band structure without alternating.

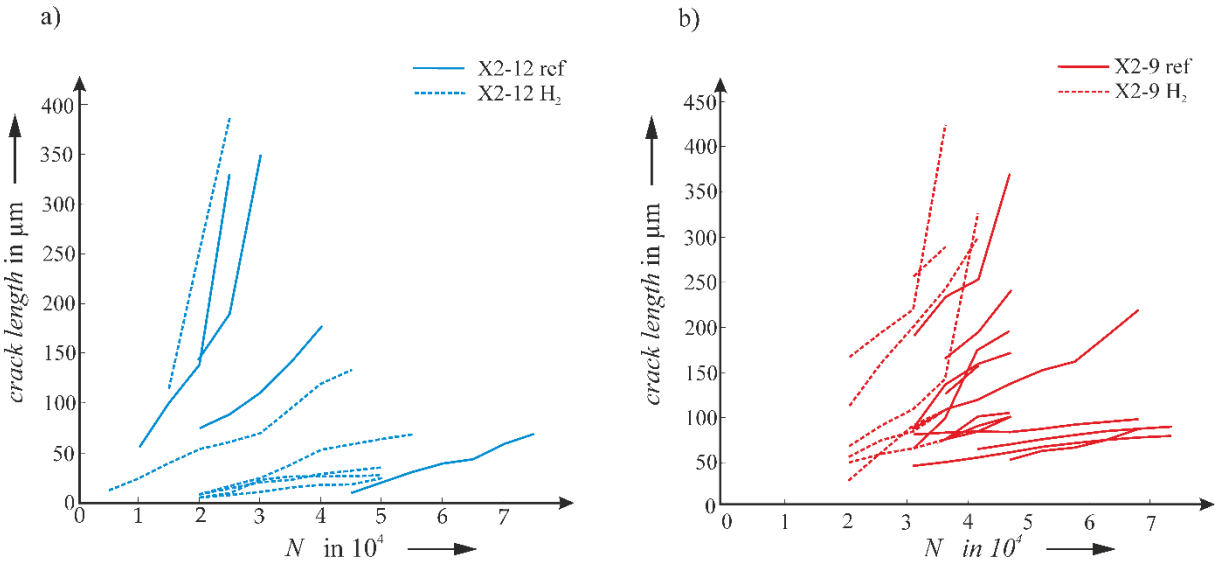

Figure 3. Fatigue crack growth curves of (**a**) X2-12 and (**b**) X2-9 in reference and precharged conditions, tested at a stress ratio of $R = -1$, $f = 1$ Hz, and a stress amplitude of 365 MPa (X2-12), 430 MPa (X2-9 H_2), and 460 MPa (X2-9 ref) [4] (reproduced from [4], MDPI, 2018).

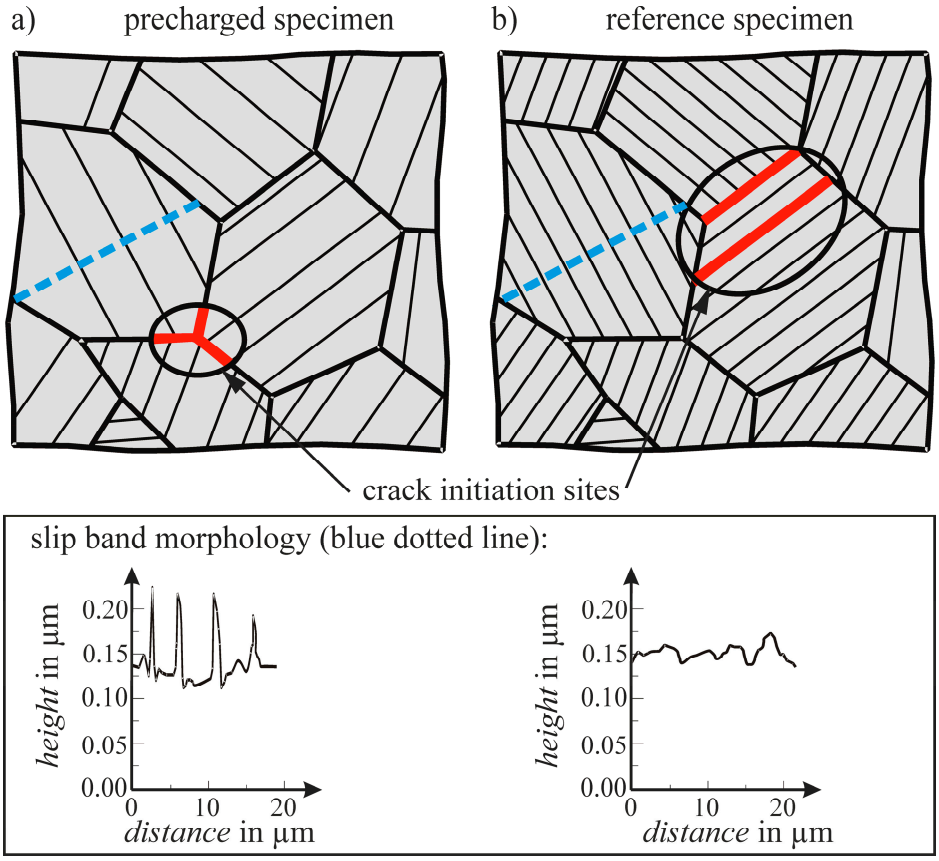

Figure 4. Schematic representation of crack initiation location and slip band morphology in (**a**) precharged and (**b**) reference specimen of X2-12 [4] (reproduced from [4], MDPI, 2018).

Additionally, the evaluation of the slip bands formed around the crack revealed clear differences between the different conditions of X2-12. While the minimum height of the slip bands is similar for both conditions, they protrude significantly higher from the surface in precharged samples (see Figure 4). Moreover, the average distance of the slip bands in

the precharged samples is about 4.7 µm, whereas in the reference samples the value is just 1.92 µm.

In the case of the X2-9 specimens, the influence of hydrogen is clearly detected in the crack growth diagrams, as depicted in Figure 3b. Despite the lower stress amplitude σ_a (430 MPa compared to 460 MPa) applied at the precharged specimens, crack growth starts earlier and is faster. Furthermore, the crack initiation site changes from grain boundaries and slip bands to grain boundary triple points, as already observed for X2-12. The crack morphology in both, the precharged and reference specimens, show an austenite-α'-martensite transformation along the crack path and in grains located close to the crack. Note that no significant differences in austenite-α'-martensite transformation were observed between the reference and the precharged specimens of X2-9.

3.2. Results Obtained with the PhyBaL$_{CHT}$ Method

As shown in [36] on differently heat treated 42CrMo4, the cyclic deformation behavior obtained in cyclic indentation is comparable to the cyclic deformation curves observed in uniaxial compressive fatigue tests. Thus, in this work, the cyclic deformation behavior of the different materials was analyzed using CITs.

Comparing the reference and the precharged conditions, the results depicted in Figure 5a, showing $h_{a,p}$-N curves obtained with a Vickers indenter and F_{max} = 1000 mN, demonstrate significant differences in the cyclic deformation behavior for both, X2-9 and X2-12. For both steels, the precharged condition shows lower $h_{a,p}$ values and hence, a lower level of plastic deformation than the reference specimens. Comparing the two steels, the X2-12 sample exhibits significantly smaller $h_{a,p}$ than the X2-9 sample in both, reference as well as precharged condition.

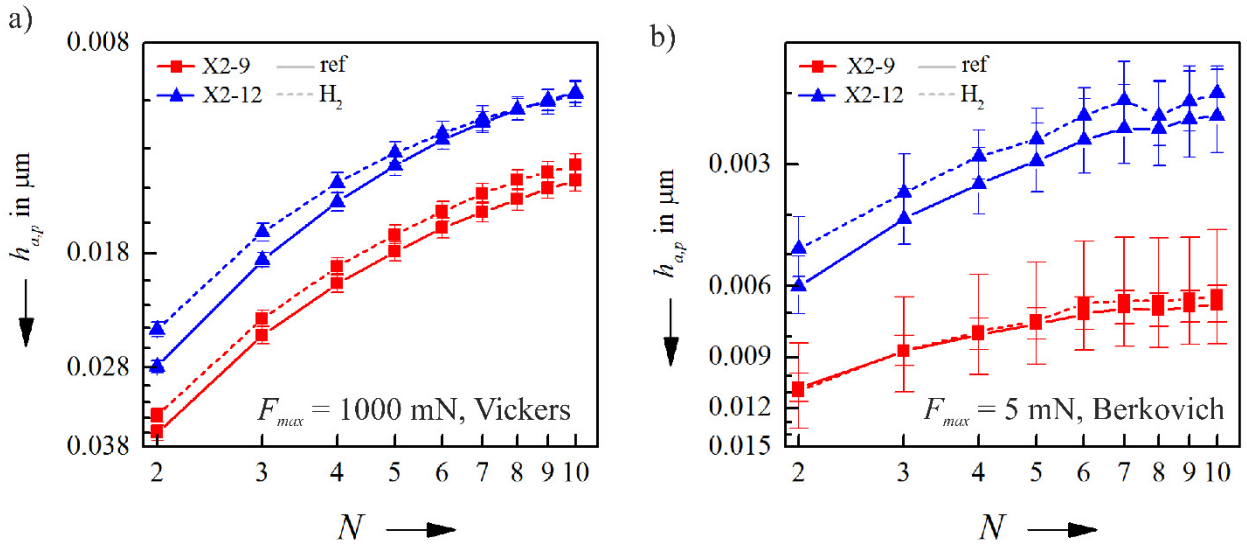

Figure 5. The *ha,p-N* curves of X2-9 and X2-12 metastable austenitic stainless steel samples in reference (ref) as well as hydrogen precharged (H_2) condition, obtained in cyclic microindentation tests with (**a**) F_{max} = 1000 mN and a Vickers indenter, as well as (**b**) F_{max} = 5 mN and a Berkovich indenter.

Similarly, the results illustrated in Figure 5b, which were obtained with a Berkovich indenter and F_{max} = 5 mN, demonstrate higher plasticity of X2-9. In contrast to the results obtained with F_{max} = 1000 mN, X2-9 exhibits nearly identical $h_{a,p}$-N curves for both, reference and precharged conditions, whereas for X2-12 lower $h_{a,p}$ are shown by the precharged condition (see Figure 5b), which is in accordance with the results obtained with higher indentation force. Moreover, a significantly higher scatter of $h_{a,p}$ values can be seen at lower indentation forces, which is caused by the greater influence of microstructural inhomogeneities resulting from the smaller indentation depth.

The high scatter of $h_{a,p}$ disables a reliable determination of the cyclic hardening exponent$_{CHT}$ and consequently, e_{II} was determined only from indentation tests performed with F_{max} = 1000 mN (see Figure 6). Nevertheless, the rating of the microhardness, determined at F_{max} = 5 mN, corresponds to the results obtained at F_{max} = 1000 mN, which is caused by the less pronounced scatter in indentation depth achieved in the first indentation cycle.

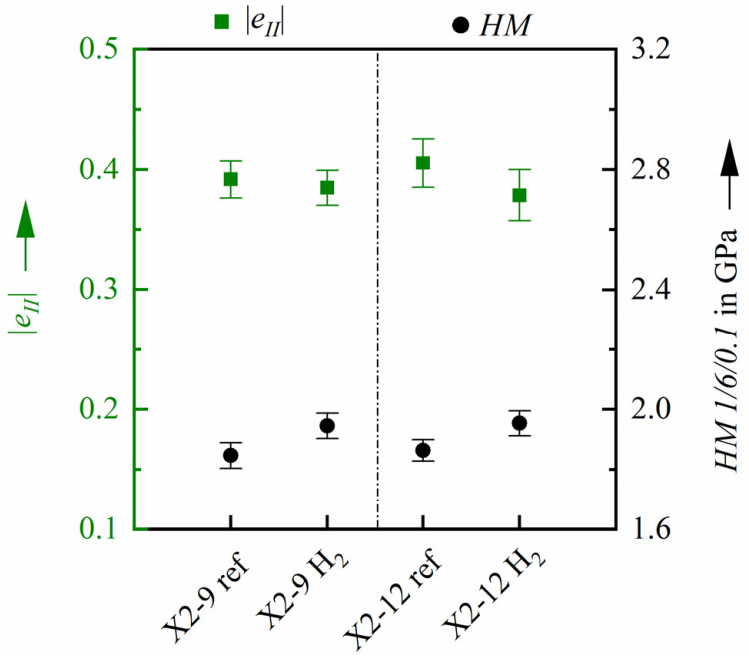

Figure 6. Comparison of the Martens hardness *HM* and the cyclic hardening exponent$_{CHT}$ e_{II} of precharged (H_2) and reference (ref) specimens of the metastable austenitic steels X2-9 and X2-12 determined at F_{max} = 1000 mN by means of the PhyBaL$_{CHT}$ method.

It has to be considered that the indentation forces used lead in addition to the significantly different indentation depth to different stress conditions as well as plastically deformed volumes, being more extended for F_{max} = 1000 mN, resulting in higher values of $h_{a,p}$. However, at an identical indentation force, the different conditions show similar maximum indentation depths and thus, comparable stress states. Consequently, the deformation behavior of the different material conditions can only be compared using the results obtained at an identical indentation force.

In Figure 6, the values of e_{II} and *HM*, which were obtained in cyclic microindentation tests performed at F_{max} = 1000 mN, are shown for X2-9 and X2-12. Despite the significant differences in austenite stability and chemical composition, both materials show comparable values of *HM* and e_{II}. As expected, the hardness of precharged specimens is increased for both materials, which was also observed with the Berkovich indenter and F_{max} = 5 mN. Furthermore, a significantly lower cyclic hardening potential of the precharged specimens is shown for the X2-12 steel (see Figure 6). For the X2-9 variant, a trend towards lower cyclic hardening potential can also be observed for the precharged specimens, which is however, significantly less pronounced in comparison to the X2-12 steel. Note that e_{II} and *HM* represent mechanical properties at different length scales. While *HM* is dominated by macroplastic deformation processes, e_{II} is a result of microplasticity at a significantly smaller length scale.

3.3. Nanoindentation Fatigue Tests

For a higher resolution of the cyclic deformation processes down to nanoscale, nanoindentation fatigue tests were conducted with a static load of 100 µN and a load amplitude

of 80 µN, resulting in a significantly lower indentation depth and thus, a smaller plastically deformed zone compared to the microindentation tests shown in Section 3.2. As this further results in a higher influence of microstructural inhomogeneities, 10 indentations were performed for each condition to determine a representative deformation behavior, respectively. Note that the indentation depths observed at mean loading were at comparable length scales for the different material conditions, leading to comparable stress conditions.

In the nanoindentation fatigue tests only the displacement amplitude was determined, which is shown exemplarily in Figure 7. Comparing the reference and precharged specimens, a trend towards a higher level of displacement amplitude can be observed for precharged variants of both materials, caused by a more pronounced plastic deformation beneath the indenter.

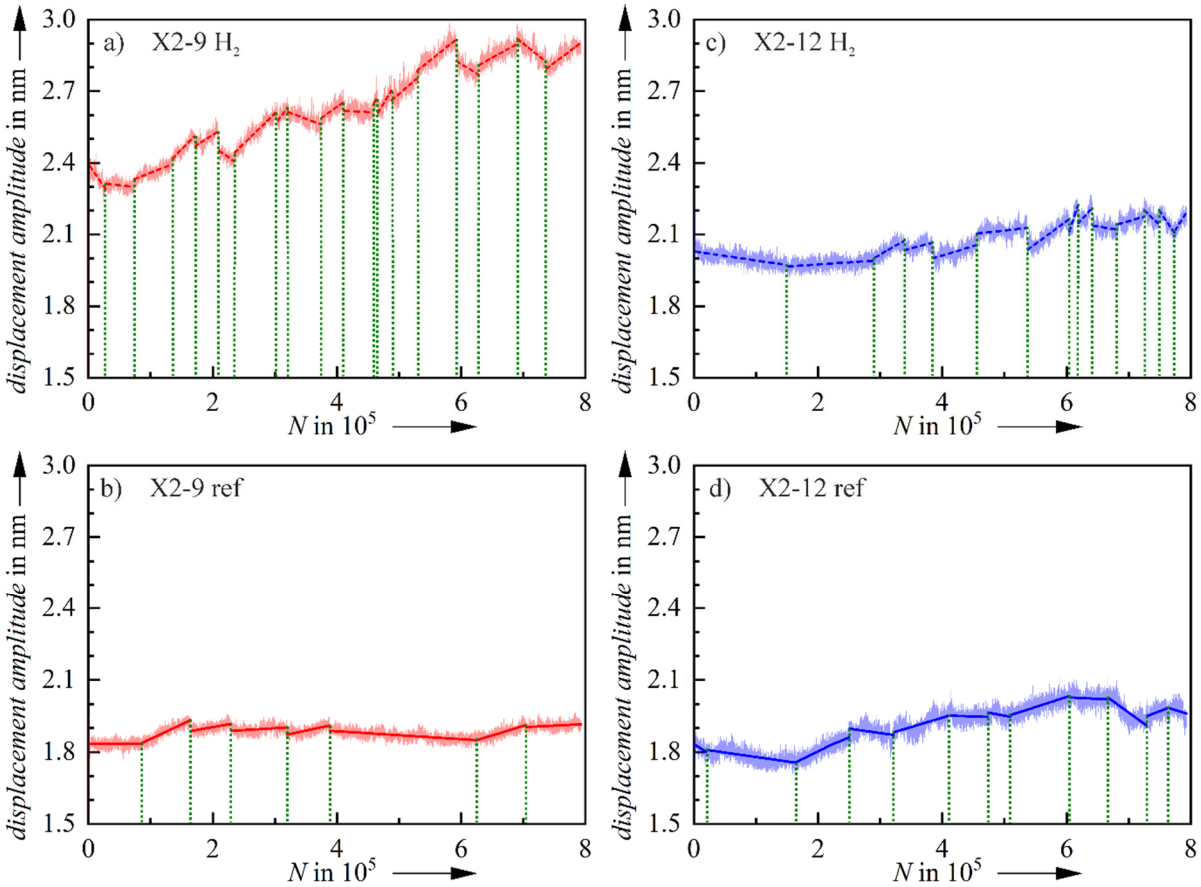

Figure 7. Examples of *displacement amplitude-N* curves including the definition of *events* for (**a**) X2-9 H_2, (**b**) X2-9 ref, (**c**) X2-12 H_2 and (**d**) X2-12 ref.

Comparing the number of *events* in the course of the displacement amplitude, represented by the green dotted lines in Figure 7 and defined as abrupt changes in displacement amplitude, significant differences can be observed. The precharged specimens show significantly more *events*, which represent more pronounced plastic deformation [41]. In Figure 8, for each steel the number of *events* is given in relation to the maximum number of *events* measured in precharged conditions. Note that a high scatter was observed in these experiments, leading to a relatively high standard deviation (see Figure 8). However, the mean values indicate that the precharged specimens exhibit a significantly higher number of *events* than the reference variants. As the *events* are assumed to be caused by the movement of dislocations, this indicates a greater local plastic deformation of hydrogen precharged specimens.

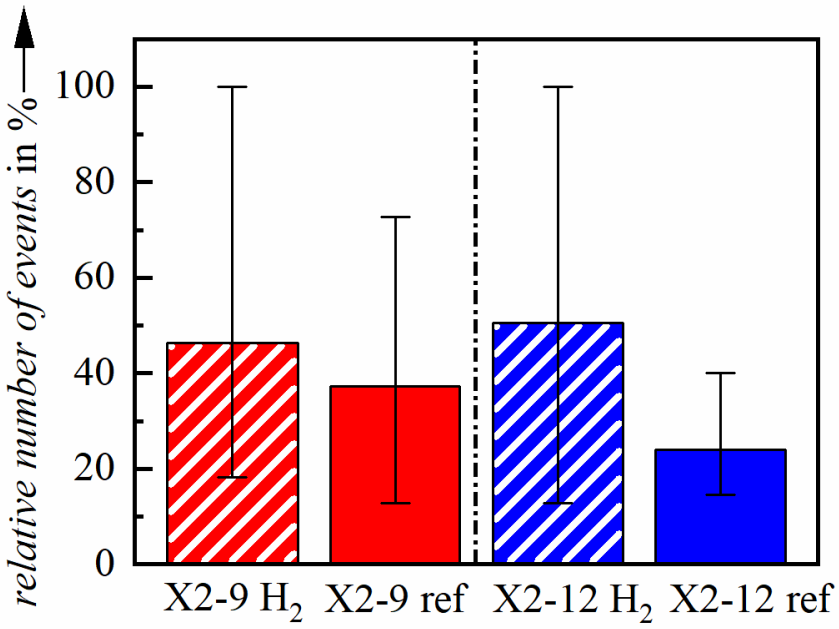

Figure 8. Number of events observed in different material conditions of X2-9 and X2-12, in relation to their respective hydrogen precharged variants.

3.4. TEM Analyzes

For an investigation of the dislocation arrangements formed close to the tip of fatigue cracks of the tested fatigue specimens, and thus, in the plastically deformed volume, TEM samples were prepared by the focused ion beam technique. The samples were taken at a fatigue crack length of about 300 µm, which corresponds to approximately 20,000 cycles for precharged samples and 60,000 cycles for reference samples. Note that the TEM analyses as well as indentation tests were used to investigate the differences in cyclic deformation behavior and thus, crack propagation at microscale and nanoscale. Therefore, TEM lamellae were taken from the vicinity of a fatigue crack rather than an indent.

In both, precharged and reference condition of X2-12, cellular dislocation structures dominate the microstructure within the vicinity of the crack tip (see Figure 9). However, the average cell diameter is significantly different between the hydrogen precharged and reference condition. For the reference sample of X2-12, an average diameter of roughly 0.21 µm was measured within the first 2 µm around the crack tip, while the average cell diameter for the precharged sample was found to be about 0.49 µm and thus, being roughly two times bigger. Expanding the region analyzed up to 5 µm around the crack tip, the mean value increases for both conditions of X2-12. While the mean diameter of the cell structures of the reference sample rises to 0.58 µm, the TEM lamella from the precharged sample exhibits an average diameter of about 1.14 µm, which also means a factor of approximately two between the reference and precharged condition. As shown in Figure 9, the crack propagates along the sub-grain boundaries and due to the larger cells of the precharged condition, the crack alternates are more pronounced compared to the reference sample. In addition to the difference in cell diameter, the reference samples show a cell structure across the whole lamella, whereas the cell structure of the precharged sample is limited to an area of about 7 µm around the crack tip and hence, is more localized (compare Figure 9a,b).

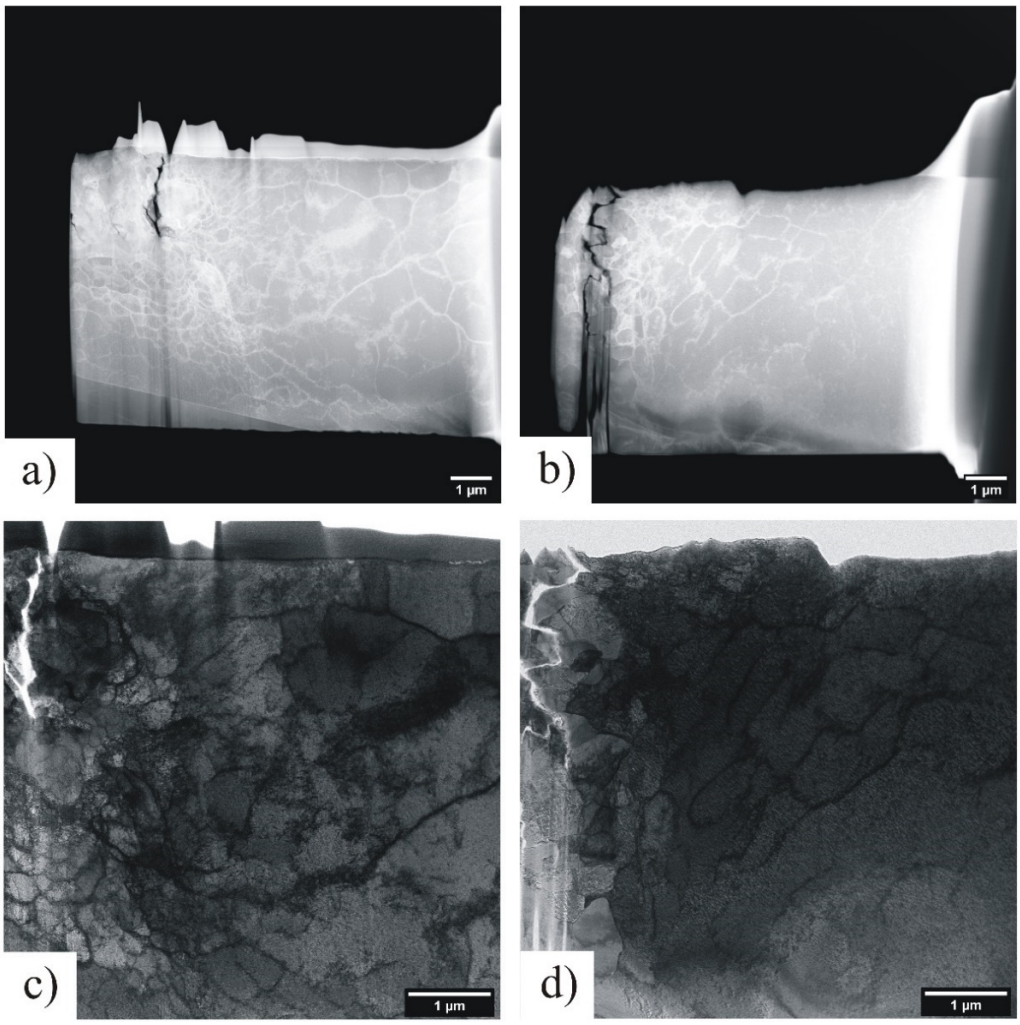

Figure 9. TEM results of X2-12: (**a**) And (**b**) are overview STEM images showing the position of the crack tip for (**a**) the reference and (**b**) the precharged condition; (**c**) and (**d**) are corresponding TEM bright-field images at higher magnification documenting dislocation cells.

For the less stable X2-9, the fatigue behavior was dominated by deformation-induced phase transformation for both, reference and precharged condition (see Figure 10). In the TEM micrographs of the reference sample, typical rod-like structures are visible, which are aligned along a preferred growth direction. In addition to the folding of small crystallographic areas, the formation of deformation twins is also observable. Moreover, dislocations accumulate at the phase boundaries between the austenitic matrix and the newly formed α'-martensite. The TEM lamellae from the precharged condition shows microstructural features similar to the reference sample. Fatigue loading also results in the formation of body centered cubic (BCC) α'-martensite and thus, pronounced phase boundaries are visible between martensitic regions and the austenitic phase. Additionally, dislocations accumulate along the phase boundaries in the precharged X2-9 sample, which correlates to the observations at reference variant of X2-9. In summary, the differences between the precharged and reference condition observed in TEM analyses are significantly less pronounced for X2-9 compared to X2-12.

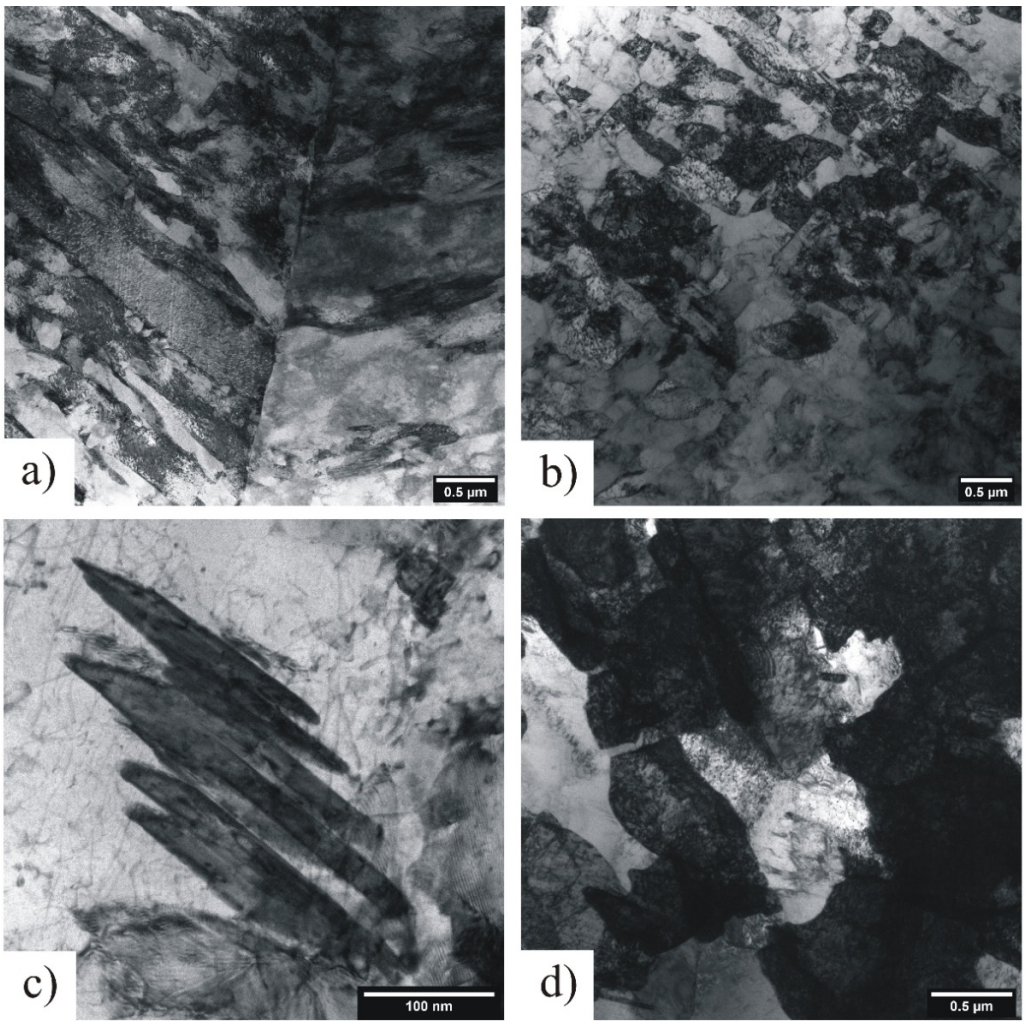

Figure 10. TEM bright-field images of X2-9: (**a**,**c**) In the reference condition and (**b**,**d**) in the precharged condition.

4. Discussion

4.1. Fatigue Crack Initiation and Propagation

As the conclusions drawn from the fatigue tests are the motivation of the cyclic indentation testing and TEM analyses shown in the present work, they are given compactly in the following and are discussed in more detail in the already published work [4]. The fatigue tests on X2-12 specimens (see Figure 3a and [4]) showed no clear influence of hydrogen on the crack growth rate, which is probably a consequence of the high scatter observed. Nevertheless, an effect of hydrogen was found in the form of a change in the crack initiation site and the crack path morphology. The crack initiation site changes from commonly observed slip bands and grain boundaries to grain boundary triple points. As microstructural defects and their tensile stress fields are generally known as hydrogen traps [42], this is in accordance to the HEDE mechanism as boundary triple points represent larger defects than single grain boundaries and, consequently, attract more hydrogen [4].

However, the HEDE mechanism cannot explain the difference observed in the slip band height and distance caused by hydrogen, which is in accordance with the reports of Robertson et al. [17] on AISI 310 s. The changes in the slip band morphology observed are caused by a localization of plastic deformation [4]. The HELP mechanism could explain these phenomena in terms of a hydrogen-induced reduction of the yield stress, enabling both, easier and more localized dislocation movement [4].

In contrast to X2-12, the crack growth curves of X2-9 revealed a clear influence of hydrogen (see Figure 3b). The fact that the steel X2-9 is more susceptible to hydrogen than X2-12 accords well with the literature, which states that the tendency to hydrogen embrittlement increases with the reduced Ni content. The smaller Ni content leads to a lower stacking fault energy, a higher hydrogen diffusion rate as well as a lower austenite stability and thus, an increased content of deformation-induced α'-martensite [43]. However, this alone does not provide information of the relevant hydrogen embrittlement mechanism. The influence on the crack growth rate is more pronounced for X2-9, since it forms more α'-martensite along and in front of the fatigue crack, allowing additional hydrogen to quickly reach the crack tip due to the higher diffusion coefficient, which results in faster crack growth [4]. Consequently, the amount of hydrogen in the vicinity of the crack tip is assumed to be higher at X2-9 than at X2-12, leading to a more pronounced effect of hydrogen embrittlement. However, the relevant mechanisms are expected to be on a small scale, which has to be verified by using mechanical testing on a significantly smaller scale.

To investigate the effects of hydrogen on the cyclic deformation behavior on a small scale, in the present work cyclic indentation tests have been performed. Moreover, this was combined by TEM investigations in the vicinity of fatigue cracks observed for the different materials and conditions to analyze the interrelation between hydrogen effects, dislocation movement, and the local cyclic deformation behavior.

4.2. Local Cyclic Deformation Behavior in Indentation Tests

The results obtained with F_{max} = 1000 mN show significant differences in the cyclic deformation behavior of precharged and reference condition for X2-9 as well as X2-12. The generally lower level of plastic deformation and higher hardness observed for precharged specimens (see Figures 5a and 6) are in accordance with many other research works [19–24]. However, in almost all of these studies stable austenitic stainless steels were examined, for which the influence of hydrogen is considered without phase transformation, which is locally enhanced due to hydrogen precharging [44]. In the present work, both effects, phase transformation and hydrogen solid solution hardening, have to be considered. Note that the determination of microhardness is related to massive plastic deformation processes in a relatively large volume beneath the indenter (comp. [36]) and, therefore, the localized influence of the HELP mechanism can be disregarded. However, the hardness measurements are based on macroplastic deformation and represent the deformation behavior of the material on a relatively big scale.

As the cyclic hardening exponent$_{\mathrm{CHT}}$ e_{II} is based on the deformation behavior at a higher number of cycles and thus, on microplastic deformation processes, this value can be used for analyses on the microscale, which can be correlated to local effects. The lower cyclic hardening potential of precharged specimens, represented by smaller $|e_{II}|$ (see Figure 6), can also be explained by hydrogen effects. It is assumed that the HELP mechanism leads to an increased dislocation mobility at microstructural obstacles in the precharged samples and consequently, to a lower capability of the material to stop the dislocation movement, thereby decreasing the local cyclic hardening potential. As the influence of the HELP mechanism increases at more localized deformation, the cyclic hardening potential of precharged specimens is decreased, while their hardness is slightly higher in relation to the reference condition. The effect of decreased cyclic hardening potential caused by hydrogen is less pronounced for X2-9, which might be caused by superimposition of the enhanced phase transformation. As a more pronounced phase transformation leads to a higher cyclic hardening potential, this is assumed to counteract the effects of HELP mechanism, which cannot be clarified finally with the presented results.

In the additionally performed nanoindentation fatigue tests, which enable a substantially higher spatial resolution than the microindentation tests, for both materials the precharged specimens exhibit a greater number of *events* as well as an increased displacement amplitude in relation to the reference samples. Due to the very low maximum indentation force of 180 µN, displacement amplitudes in the range of nanometers were

achieved. This is referred to very localized deformation processes on the nanoscale, and thus, the HELP mechanism is assumed to be the dominant hydrogen-induced effect. Consequently, both steels show higher plastic deformability in the precharged condition. Note that the abrupt changes of the displacement amplitude can be attributed to local dislocation movements, which are enhanced by hydrogen according to the HELP mechanism.

The indentation tests reveal significantly higher plasticity of precharged specimens at microscale and nanoscale, which correspond to the assumption of activity of HELP mechanism at these length scales. These results can be correlated to the local deformation processes occurring in the small plastically deformed volume in front of the crack tip, showing also high stress intensities. Consequently, the results obtained in indentation testing indicate the activity of HELP mechanism during fatigue crack propagation, which is in accordance with the differences in slip band morphology observed. It is worth mentioning that the cyclic indentation tests reveal the hydrogen effects clearly for both steels, while fatigue crack propagation rates only show an influence for X2-9.

4.3. TEM Analyses

Since microindentation and nanoindentation tests revealed that the presence of hydrogen locally causes a significant increase in dislocation mobility, TEM lamellae were extracted in front of the crack tips from reference and precharged specimens of both steels. This enables an investigation of the dislocation arrangements in the plastically deformed volume in front of the crack tip and thus, the analysis of dislocation mobility during fatigue crack propagation.

The TEM analyses on steel X2-12 present qualitatively similar dislocation structures near the crack tip for reference and precharged samples. Within areas of strong plastic deformation, the formation of characteristic cell structures could be observed, which corresponds to [45]. Towards the immediate vicinity of the crack tip, where the material suffers maximum stresses, the cell diameter significantly decreases, which indicates an increase in stress level with decreasing distance to the crack tip. Although internal hydrogen does not suppress the formation of dislocation cells at the crack tip, the extent of cell formation is reduced. The coarser cells found in precharged specimens can be attributed to the increased dislocation mobility, resulting from the presence of solved hydrogen. Rather than forming fine cell walls, the dislocations can travel longer distances per loading half-cycle, which can be attributed to the HELP mechanism and leads to a larger cell diameter. This coarser cell structure leads to an unsteady crack growth, since the fatigue crack propagates along the cell boundaries [4] as schematically represented in Figure 11a. For the uncharged reference samples, the lower dislocation mobility leads to the formation of small cells and thus, to a more straight-lined crack growth. In addition to the difference in cell size, the extent of the area that shows the dislocation cell arrangement is affected by hydrogen. In comparison to the reference samples, the precharged samples exhibit a more localized cellular area in front of the crack tip, resulting from more localized plastic deformation. The enhanced local plastic deformation correlates well with the results obtained in indentation tests. Consequently, the presented results demonstrate that the indentation approaches used, i.e., PhyBaL_{CHT} and nanoindentation fatigue tests, are powerful means to analyze the hydrogen-induced effects on the cyclic deformation behavior on a local level.

For the crack initiation process in the hydrogen precharged condition, it is assumed that antecedent to the crack initiation HELP provides an accumulation of dislocations at the grain boundaries, resulting in a locally increased hydrogen content caused by more pronounced distortion of the lattice. This is expected to lead to a high local concentration of hydrogen at the grain boundary triple point, which results in crack initiation caused by HEDE, as higher hydrogen contents provide decohesion [14]. After this, the HELP mechanism is expected to be active in the plastically deformed volume in front of the crack tip, which is supported by TEM analyses and cyclic indentation tests. This leads to coarser dislocations cells, and thus, significantly changes the crack path morphology in

relation to the reference condition, as the fatigue crack propagates along the dislocation cell boundaries.

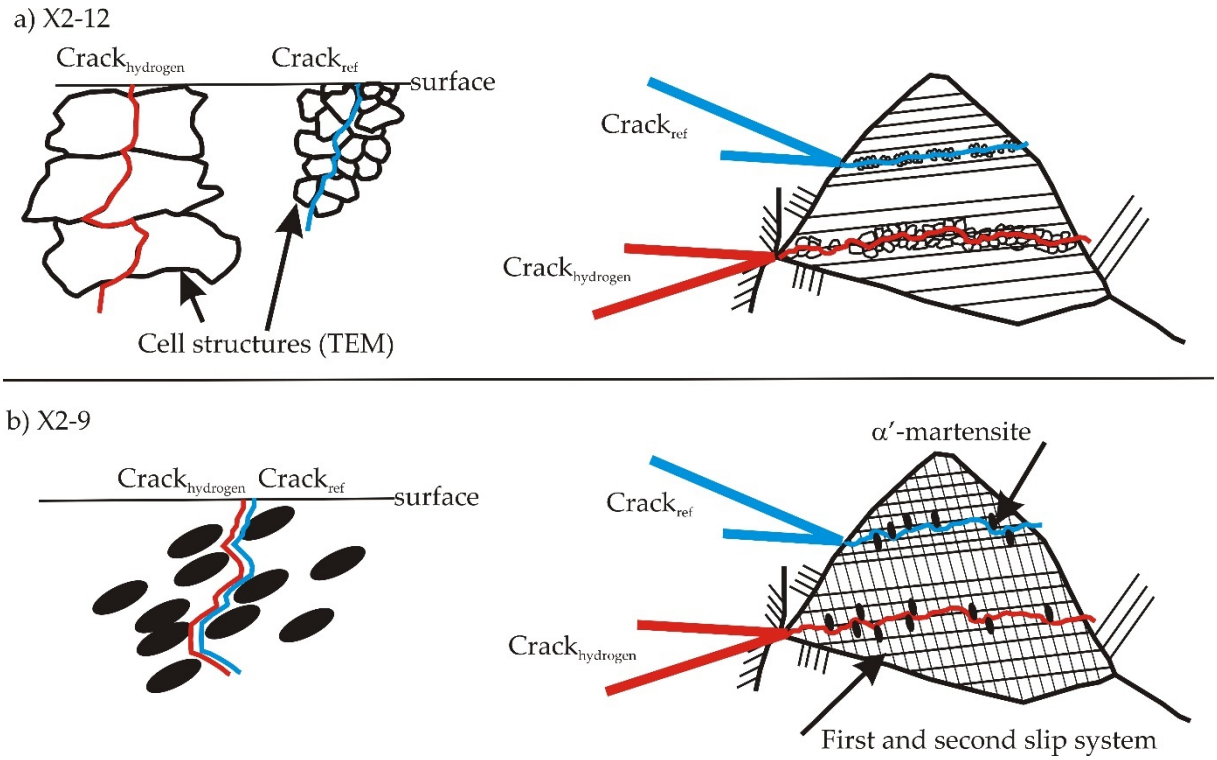

Figure 11. Schematic representation of the formation of different dislocation cell structures and crack propagation paths in reference specimens (red) and hydrogen precharged samples (blue) of (**a**) X2-12 and (**b**) X2-9.

In contrast to X2-12, the TEM analyses of reference and precharged X2-9 samples provide no significant differences. As the lower Ni content of X2-9 results in a substantially lower stacking fault energy [46], this alloy is prone to deformation-induced phase transformation during fatigue loading, while in X2-12 plastic deformation takes place in the single-phase austenitic condition [4]. The martensite plates formed in X2-9 show higher hardness and strength than the austenitic matrix. Moreover, the phase transformation is accompanied by a volume increase, leading to compressive stresses ahead of the crack tip. Consequently, the fatigue crack growth is impeded or completely suppressed. During crack growth, bypassing the martensitic particles seems to be more efficient for a crack than passing through the martensite. Therefore, an alternating crack path prevails, which is unaffected by the material conditions (compare Figure 11b).

Note that the transformation from the face centered cubic (FCC) to the BCC crystal structure strongly affects the hydrogen diffusivity of the material by 4 to 5 orders of magnitude [43], and thus, significantly enhances the diffusion rate of hydrogen. Consequently, the hydrogen is transported much faster to the crack tip at X2-9 compared to X2-12. This could explain the more pronounced difference between the precharged and the reference condition observed in the fatigue test for X2-9 in relation to X2-12. As the hydrogen concentration necessary to locally promote the HELP mechanism can be established more easier and faster in X2-9, it is assumed, that the HELP mechanism enhances the fatigue crack propagation at X2-9. This is underlined by the results obtained in indentations tests, which indicate a strong influence of the HELP mechanism. Thus, the presented results underline the potential of indentation testing for the analysis of localized hydrogen-induced effects. However, the TEM results do not indicate a modified dislocation structure as it was found in X2-12, which is presumably caused by the effects of phase transformation, disabling a thorough analysis of deformation-induced dislocation structures.

5. Summary and Conclusions

Many studies in the literature deal with the question on the relevant mechanism for the effect of hydrogen on the fatigue behavior of metallic materials. In the presented investigations, this question was addressed for two metastable austenitic stainless steels (X2-9 and X2-12) in the reference and hydrogen precharged condition, whereby hydrogen precharging was performed from the gas phase, which led to hydrogen contents of 40 wppm for X2-12 and 26 wppm for X2-9. Therefore, mechanical testing on different length scales was performed, i.e., fatigue, cyclic indentation, and nanoindentation fatigue tests, which was complemented by TEM analyses in the vicinity of the fatigue cracks. Note that the two steels investigated differ in austenite stability due to the different Ni contents (9'wt% (X2-9) and 12 wt% (X2-12)), whereby X2-9 exhibits lower austenite stability and thus, pronounced austenite-α'-martensite transformation. From the presented results, the following conclusions can be drawn:

- In accordance with the different crack morphology observed in fatigue tests, the TEM analyses at X2-12 revealed coarser dislocation cell structures for the hydrogen precharged condition, which indicate an enhanced local plasticity. The more pronounced plasticity on a local level and thus, at small (micro and nano) length scale is also shown by the cyclic indentation, as well as nanoindentation fatigue tests. The increased plasticity at these length scales can be explained with the hydrogen enhanced localized plasticity (HELP) mechanism, which is assumed to be active for X2-12 and to cause the differences in fatigue crack morphology.
- For X2-9, the TEM analyses showed no differences between the reference and hydrogen precharged condition, which is caused by pronounced phase transformation, disabling thorough analyses of deformation-induced dislocation structure. However, the indentation tests also indicate higher local plasticity for the precharged condition of X2-9. Consequently, also for X2-9 the HELP mechanism is assumed to be active during fatigue crack propagation. Combined with the increased diffusion rate after phase transformation, resulting in a higher amount of hydrogen in the vicinity of the crack tip, the HELP mechanism is expected to lead to a significantly faster crack propagation rate of precharged condition compared to the hydrogen-free material.
- The indentation tests performed in this work enabled a valid analysis of the influence of hydrogen on the local cyclic deformation behavior and consequently, the presented indentation testing approaches are powerful means for analyzing hydrogen-induced effects on a local level.

As a summary, the results obtained at different length scales in the framework of the presented study indicate that the HELP mechanism explains the hydrogen-induced intrinsic fatigue crack propagation phenomena observed. However, considering the fatigue tests performed in the preliminary work, the fatigue crack initiation seems to be dominated by the hydrogen enhanced decohesion (HEDE) mechanism. Thus, the dominating mechanism of hydrogen embrittlement is assumed to change during the fatigue lifetime of the investigated materials, which is in accordance with research on other austenitic steels. Due to the high complexity of the crack initiation process, more detailed research has to be performed to verify this assumption.

Author Contributions: Conceptualization, S.B., B.B. (Bastian Blinn), K.D., H.-J.C., T.B., T.S., X.J., B.B. (Benjamin Butz) and S.W.; methodology, S.B., B.B. (Bastian Blinn), K.D. and M.S.; validation, S.B., B.B. (Bastian Blinn) and K.D.; formal analysis, S.B., B.B. (Bastian Blinn) and K.D.; investigation, S.B., B.B. (Bastian Blinn), K.D., Y.W. and J.M.; resources, H.-J.C., T.B., B.B. (Benjamin Butz) and S.W.; writing—original draft preparation, S.B. and B.B. (Bastian Blinn); writing—review and editing, K.D., Y.W., J.M., M.S., H.-J.C., T.B., T.S., X.J., B.B. (Benjamin Butz) and S.W.; visualization, S.B., B.B. (Bastian Blinn) and K.D.; supervision, H.-J.C., T.B. and B.B. (Benjamin Butz); project administration, H.-J.C.; funding acquisition, H.-J.C. and S.W. All authors have read and agreed to the published version of the manuscript.

Funding: This research was funded by the German Research Foundation (Deutsche Forschungsgemeinschaft: DFG) and "Forschungsvereinigung Verbrennungskraftmaschinen (FVV)".

Institutional Review Board Statement: Not applicable.

Informed Consent Statement: Not applicable.

Data Availability Statement: The data presented in this study are available on request from the corresponding author. The data are not publicly available due to ongoing research.

Acknowledgments: Part of this work was undertaken at the Micro and Nanoanalytics Facility (MNaF) of the University of Siegen, which is gratefully acknowledged.

Conflicts of Interest: The authors declare no conflict of interest. The funders had no role in the design of the study; in the collection, analyses, or interpretation of data; in the writing of the manuscript, or in the decision to publish the results.

References

1. Lynch, S. Hydrogen embrittlement phenomena and mechanisms. *Corros. Rev.* **2012**, *30*, 105–123. [CrossRef]
2. Beachem, C.D. A new model for hydrogen-assisted cracking (hydrogen "embrittlement"). *Metall. Mater. Trans. B* **1972**, *3*, 441–455. [CrossRef]
3. Pöpperling, R.; Schwenk, W. Einflußgrößen der H-induzierten Spannungsrißkorrosion bei niedriglegierten Stählen. *Mater. Corros.* **1980**, *31*, 15–20. [CrossRef]
4. Brück, S.; Schippl, V.; Schwarz, M.; Christ, H.-J.; Fritzen, C.-P.; Weihe, S. Hydrogen Embrittlement Mechanism in Fatigue Behavior of Austenitic and Martensitic Stainless Steels. *Metals* **2018**, *8*, 339. [CrossRef]
5. Petch, N.J.; Stables, P. Delayed Fracture of Metals under Static Load. *Nature* **1952**, *169*, 842–843. [CrossRef]
6. Cotterill, P. The hydrogen embrittlement of metals. *Prog. Mater. Sci.* **1961**, *9*, 205–301. [CrossRef]
7. Griffiths, A.J.; Turnbull, A. On the effective diffusivity of hydrogen in low alloy steels. *Corros. Sci.* **1995**, *37*, 1879–1881. [CrossRef]
8. Lynch, S.P. Hydrogen embrittlement and liquid-metal embrittlement in nickel single crystals. *Scr. Metall.* **1979**, *13*, 1051–1056. [CrossRef]
9. Lynch, S.P. Environmentally assisted cracking: Overview of evidence for an adsorption-induced localised-slip process. *Acta Metall.* **1988**, *36*, 2639–2661. [CrossRef]
10. Lynch, S.P. Metallographic contributions to understanding mechanisms of environmentally assisted cracking. *Metallography* **1989**, *23*, 147–171. [CrossRef]
11. Lynch, S.P. Comments on "A unified model of environment-assisted cracking". *Scr. Mater.* **2009**, *61*, 331–334. [CrossRef]
12. Wang, Y.; Wang, X.; Gong, J.; Shen, L.; Dong, W. Hydrogen embrittlement of catholically hydrogen-precharged 304L austenitic stainless steel: Effect of plastic pre-strain. *Int. J. Hydrog. Energy* **2014**, *39*, 13909–13918. [CrossRef]
13. Li, X.; Gong, B.; Deng, C.; Li, Y. Failure mechanism transition of hydrogen embrittlement in AISI 304 K-TIG weld metal under tensile loading. *Corros. Sci.* **2018**, *130*, 241–251. [CrossRef]
14. Djukic, M.B.; Bakic, G.M.; Zeravcic, V.S.; Sedmak, A.; Rajicic, B. The synergistic action and interplay of hydrogen embrittlement mechanisms in steels and iron: Localized plasticity and decohesion. *Eng. Fract. Mech.* **2019**, *216*, 106528. [CrossRef]
15. Zhao, Y.; Seok, M.-Y.; Choi, I.-C.; Lee, Y.-H.; Park, S.-J.; Ramamurty, U.; Suh, J.-Y.; Jang, J.-i. The role of hydrogen in hardening/softening steel: Influence of the charging process. *Scr. Mater.* **2015**, *107*, 46–49. [CrossRef]
16. Weidner, A.; Biermann, H. Case studies on the application of high-resolution electron channelling contrast imaging–investigation of defects and defect arrangements in metallic materials. *Philos. Mag.* **2015**, *95*, 759–793. [CrossRef]
17. Lynch, S.P. Revealing the fundamental processes controlling hydrogen embrittlment. In *Effects of Hydrogen on Materials, Proceedings of the 2008 International Hydrogen Conference, WY, USA, 7–10 September 2008*; Somerday, B., Sofronis, P., Jones, R., Eds.; ASM International: Cleveland, OH, USA, 2009.
18. Gerberich, W.W.; Marsh, P.G.; Hoehn, J.W.; Venkataraman, S.; Huang, H. Hydrogen/plasticity interactions in stress corrosion cracking. *Corros. Deform. Interact.* **1993**, 325–353.
19. Nibur, K.; Bahr, D.; Somerday, B. Hydrogen effects on dislocation activity in austenitic stainless steel. *Acta Mater.* **2006**, *54*, 2677–2684. [CrossRef]
20. Barnoush, A.; Asgari, M.; Johnsen, R. Resolving the hydrogen effect on dislocation nucleation and mobility by electrochemical nanoindentation. *Scr. Mater.* **2012**, *66*, 414–417. [CrossRef]
21. Godoi, W.; Kuromoto, N.K.; Guimarães, A.S.; Lepienski, C.M. Effect of the hydrogen outgassing time on the hardness of austenitic stainless steels welds. *Mater. Sci. Eng. A* **2003**, *354*, 251–256. [CrossRef]
22. Iost, A.; Vogt, J.B. Hardness variation in a cathodic hydrogen-charged austenitic stainless steel. *Scr. Mater.* **1997**, *37*, 1499–1504. [CrossRef]
23. Zhang, L.; An, B.; Iijima, T.; Marchi, C.S. Effect of Gaseous Hydrogen Charging on Nanohardness of Austenitic Stainless Steels. In *Proceedings of the ASME 2016 Pressure Vessels and Piping Conference, Vancouver, BC, Canada. Volume 6B: Materials and Fabrication*; ASME: New York, NY, USA, 2016.

24. Hong, Y.; Zhou, C.; Zheng, Y.; Zhang, L.; Zheng, J.; An, B.; Chen, X.; Wang, X. Hydrogen effect on the deformation evolution process in situ detected by nanoindentation continuous stiffness measurement. *Mater. Charact.* **2017**, *127*, 35–40. [CrossRef]
25. Mine, Y.; Horita, Z.; Murakami, Y. Effect of hydrogen on martensite formation in austenitic stainless steels in high-pressure torsion. *Acta Mater.* **2009**, *57*, 2993–3002. [CrossRef]
26. Pharr, G.M. Measurement of mechanical properties by ultra-low load indentation. *Mater. Sci. Eng. A* **1998**, *253*, 151–159. [CrossRef]
27. Oliver, W.C.; Pharr, G.M. Measurement of hardness and elastic modulus by instrumented indentation: Advances in understanding and refinements to methodology. *J. Mater. Res.* **2004**, *19*, 3–20. [CrossRef]
28. Xu, B.X.; Yue, Z.F.; Wang, J. Indentation fatigue behaviour of polycrystalline copper. *Mech. Mater.* **2007**, *39*, 1066–1080. [CrossRef]
29. Xu, B.; Yue, Z.; Chen, X. An indentation fatigue depth propagation law. *Scr. Mater.* **2009**, *60*, 854–857. [CrossRef]
30. Saraswati, T.; Sritharan, T.; Mhaisalkar, S.; Breach, C.D.; Wulff, F. Cyclic loading as an extended nanoindentation technique. *Mater. Sci. Eng. A* **2006**, *423*, 14–18. [CrossRef]
31. Kramer, H.S.; Starke, P.; Klein, M.; Eifler, D. Cyclic hardness test PHYBAL$_{CHT}$–Short-time procedure to evaluate fatigue properties of metallic materials. *Int. J. Fatigue* **2014**, *63*, 78–84. [CrossRef]
32. Görzen, D.; Schwich, H.; Blinn, B.; Song, W.; Krupp, U.; Bleck, W.; Beck, T. Influence of Cu precipitates and C content on the defect tolerance of steels. *Int. J. Fatigue* **2021**, *144*, 106042. [CrossRef]
33. Nix, W.D.; Gao, H. Indentation size effects in crystalline materials: A law for strain gradient plasticity. *J. Mech. Phys. Solids* **1998**, *46*, 411–425. [CrossRef]
34. Durst, K.; Backes, B.; Göken, M. Indentation size effect in metallic materials: Correcting for the size of the plastic zone. *Scr. Mater.* **2005**, *52*, 1093–1097. [CrossRef]
35. Sadrabadi, P.; Durst, K.; Göken, M. Study on the indentation size effect in CaF2: Dislocation structure and hardness. *Acta Mater.* **2009**, *57*, 1281–1289. [CrossRef]
36. Blinn, B.; Görzen, D.; Klein, M.; Eifler, D.; Beck, T. PhyBaL$_{CHT}$–Influence of indentation force on the results of cyclic hardness tests and investigations of comparability to uniaxial fatigue loading. *Int. J. Fatigue* **2019**, *119*, 78–88. [CrossRef]
37. Blinn, B.; Klein, M.; Gläßner, C.; Smaga, M.; Aurich, J.; Beck, T. An Investigation of the Microstructure and Fatigue Behavior of Additively Manufactured AISI 316L Stainless Steel with Regard to the Influence of Heat Treatment. *Metals* **2018**, *8*, 220. [CrossRef]
38. Grigorescu, A.C.; Hilgendorff, P.-M.; Zimmermann, M.; Fritzen, C.-P.; Christ, H.-J. Cyclic deformation behavior of austenitic Cr–Ni-steels in the VHCF regime: Part I–Experimental study. *Int. J. Fatigue* **2016**, *93*, 250–260. [CrossRef]
39. Angel, T. Formation of martensite in austenitic stainless steel-Effects of deformation, temperature and composition. *J. Iron Steel Inst.* **1954**, *177*, 165–174.
40. Schramm, R.E.; Reed, R.P. Stacking fault energies of seven commercial austenitic stainless steels. *Metall. Trans. A* **1975**, *6*, 1345–1351. [CrossRef]
41. Faisal, N.H.; Prathuru, A.K.; Goel, S.; Ahmed, R.; Droubi, M.G.; Beake, B.D.; Fu, Y.Q. Cyclic Nanoindentation and Nano-Impact Fatigue Mechanisms of Functionally Graded TiN/TiNi Film. *Shape Mem. Superelasticity* **2017**, *3*, 149–167. [CrossRef]
42. Kesten, M.; Gräfen, H. Druckwasserstoffangriff auf unlegierte und niedriglegierte Stähle im Temperaturbereich unterhalb 200 C. In *Wasserstoff und Korrosion*, 2nd ed.; Kuron, D., Ed.; Bonner Studien Reihe: Bonn, Germany, 2000; pp. 101–126.
43. Pircher, H.; Großterlinden, R. Wasserstoffinduzierte Korrosion von niedriglegierten Stählen in wäßrigen Medien. *Mater. Corros.* **1987**, *38*, 57–64. [CrossRef]
44. Murakami, Y.; Kanezaki, T.; Mine, Y. Hydrogen Effect against Hydrogen Embrittlement. *Metall. Trans. A* **2010**, *41*, 2548–2562. [CrossRef]
45. Christ, H.-J. Materialermüdung und Werkstoffmikrostruktur. In *Ermüdungsverhalten Metallischer Werkstoffe*; Christ, H.-J., Ed.; Wiley-VCH: Weinheim, Germany, 2009; pp. 35–51.
46. Pontini, A.E.; Hermida, J.D. X-Ray diffraction measurement of the stacking fault energy reduction induced by hydrogen in an AISI 304 steel. *Scr. Mater.* **1997**, *37*, 1831–1837. [CrossRef]